Int. J. Electrochem. Sci., 13 **(2018)** 9950 – 9963, doi: 10.20964/2018.10.15

International Journal of
ELECTROCHEMICAL
SCIENCE
www.electrochemsci.org

Facile Synthesis of Ni-doped Nano-$LiMn_2O_4$ ($0 \leq x \leq 0.10$) Cathode Materials and Their Electrochemical Performances

Yue Yu[1,2,3], *Shimin Wang*[1,2,3], *Junming Guo*[1,2,3,*], *Changwei Su*[1,2,3,*], *Xiaofang Liu*[1,2,3], *Wei Bai*[1,2,3], *Hongli Bai*[1,2,3], *Rui Wang*[1,2,3]

[1] Key Laboratory of Comprehensive Utilization of Mineral Resources in Ethnic Regions, Yunnan Minzu University, Kunming 650500, China
[2] Key Laboratory of Resource Clean Conversion in Ethnic Regions, Education Department of Yunnan, Yunnan Minzu University, Kunming 650500, China
[3] Joint Research Centre for International Cross-border Ethnic Regions Biomass Clean Utilization in Yunnan, Yunnan Minzu University, Kunming 650500, China
[*]E-mail: guojunming@tsinghua.org.cn, ying_xinsheng@163.com

Received: 4 June 2018 / *Accepted:* 20 July 2018 / *Published:* 1 September 2018

A series of Ni-doped nano-$LiNi_xMn_{2-x}O_4$ ($0 \leq x \leq 0.10$) cathode materials were rapidly synthesized by a one-step solution combustion method. The as-obtained materials were characterized by X-ray diffraction (XRD), scanning electron microscopy (SEM), transmission electron microscopy (TEM), X-ray photoelectron spectroscopy (XPS), etc. All the $LiNi_xMn_{2-x}O_4$ samples corresponds to spinel structure with particle size of 50-80 nm. The optimized $LiNi_{0.08}Mn_{1.92}O_4$ sample not only delivers excellent discharge capacity and improved cycling stability, but also possesses a large Li^+ diffusion coefficient ($D_{Li+} = 1.491\times10^{-11}$ $cm^2\cdot s^{-1}$) and a small activation energy ($E_a = 23.81$ $kJ\cdot mol^{-1}$). The cyclic voltammogram (CV) and electrochemical impedance spectroscopy (EIS) tests indicate that the optimized $LiNi_{0.08}Mn_{1.92}O_4$ has a good reversibility and a favorable kinetics in electrochemical reaction, whilst showing a greatly reduced charge transfer resistance. It is clearly illustrated that the Ni-doping can boost Li^+ diffusion, eliminate the disadvantageous Jahn-Teller effects and enhance the lithium ion kinetic process in the $LiMn_2O_4$.

Keywords: solution combustion method; nano-$LiMn_2O_4$; Ni-doped; Li^+ diffusion coefficient; activation energy; Jahn-Teller effects

1. INTRODUCTION

Lithium-ion batteries (LIBs) have been extensively applied in electric vehicles (EVs) and hybrid electric vehicles (HEVs) due to the high energy, high operating voltage, environmental-friendly and no

memory effect[1-5]. Spinel $LiMn_2O_4$ has been considered as one of the most promising cathode materials by virtue of its high safety and energy density, abundant resources, and environmental-friendly. Unfortunately, $LiMn_2O_4$ remains sever capacity decay during the charge-discharge cycling process, especially at elevated temperature (≧55 ℃) [6,7]. Many studies have approved that the capacity fading was caused by various factors, such as Jahn-Teller distortion, disproportionated reaction of Mn^{3+} ($Mn^{3+}\rightarrow Mn^{2+}+Mn^{4+}$), the two-phase unstable reaction and non-uniform partial size[8,9]. In order to restrain the Jahn-Teller distortion, cation doping has been widely considered as an effective way to improve cycle performance of the spinel $LiMn_2O_4$. Some transition and non-transition metal elements, such as Ni[10], Mg[11-13], Al[14-16], Cu[17], Fe[18], Cr[19], Co[20], etc. have been investigated. Among these doping elements, nickle (II) ions has been widely applied. Kunjuzwa et al [21]. synthesized $LiNi_{0.1}Mn_{1.9}O_4$ by aqueous reduction technique combined with a series of pre-processing and high-temperature calcination at 780℃ for 20 h. The as-prepared $LiNi_{0.1}Mn_{1.9}O_4$ has octahedral shape with particle size of 0.80-1.80 μm and retains 84% of its initial capacity (128mAh·g^{-1}) after 100 cycles at 0.2 C. The Li^+ diffusion coefficient of $LiNi_{0.1}Mn_{1.9}O_4$ is $6.89\times10^{-11}cm^2\cdot s^{-1}$. The $LiNi_xMn_{2-x}O_4$ (x=0, 0.1, 0.2) were synthesized via a solution-combustion technique by Mesfin et al[22]. The resultant $LiNi_xMn_{2-x}O_4$ materials have the typical spinel structure with the particle sizes of 3.4-10 μm. The $LiNi_xMn_{2-x}O_4$ (x=0.1, 0.2) samples retained 99% of their respective first cycle after 100 cycles, and the R_{ct} of the $LiNi_{0.1}Mn_{1.9}O_4$ and $LiNi_{0.2}Mn_{1.8}O_4$ remained essentially the same after 100 cycles. Kumar Raju et al[23]. synthesized $LiNi_{0.2}Mn_{1.8}O_4$ ($LMNO_{mic}$) by a microwave-assisted solid-state reaction. The SEM show $LMNO_{mic}$ has an octahedron morphology and the particle size is about 100-200 nm. The $LMNO_{mic}$ outperformed the pristine LMNO with a specific capacity of 108 mAh·g^{-1}, retaining 80% of its initial capacity with 90% coulombic efficiency at 1 C after 100^{th} cycles. And the Li^+ diffusion coefficient calculated at 4.2 V is found to be 2.8×10^{-12} $cm^2\cdot s^{-1}$.

The above reports fully certified that the Ni-doping can enhance the electrochemical properties and lithium-ion diffusion kinetics of spinel $LiMn_2O_4$, however, the kinetic properties of the Ni-doped $LiMn_2O_4$ were not systematically investigated. In this work, we report a rapid one-step solution combustion method to synthesize the nano-$LiMn_2O_4$ cathode materials. The crystalline phase, morphology, Li^+ diffusion coefficient and activation energy of the obtained nano-$LiNi_xMn_{2-x}O_4$ cathode materials were studied in detail.

2. EXPERIMENTAL

2.1 Preparation of materials

The nano-$LiNi_xMn_{2-x}O_4$ ($0\leq x\leq0.10$) materials were prepared by a one-step solution combustion method using CH_3COO^{2-} existed in its own raw material as fuel. Firstly, $LiNO_3$ (AR, Aladin) as lithium source, $Mn(CH_3COO)_2\cdot4H_2O$ (AR, Aladin) as manganese resource and $Ni(CH_3COO)_2\cdot4H_2O$ as nickel dopant were accurately weighted according to a stoichiometric rate of Li:Mn:Ni=1: (2-x) :x (x□0.10) and add into a 300 mL crucible, respectively. Secondly, HNO_3 (AR, Keshi) solution as an auxiliary oxidant was put into the crucible. Then the crucible which filled with the mixture was removed into an

oven at 105℃ and stirred for several times using a glass rod until the mixture was dissolved thoroughly and formed an uniformly solution. Finally, the homogeneous solution was submitted into a muffle furnace for 1h at 500℃ with an air atmosphere and the nano-$LiNi_xMn_{2-x}O_4$ ($0 \leq x \leq 0.10$) materials were obtained after naturally cooling to room temperature.

2.2. Materials characterization

The synthetic materials were characterized by powder X-ray diffraction (XRD, Bruker Company) using a D8 ADVANCE diffractometer equipped with Cu Kα radiation (λ=0.15406 nm). And the measurement range was from 10°-70° at an operation current of 40 mA and voltage of 40 kV. The morphology was observed by scanning microscopy (SEM, QUANTA-200 America FEI Company) and transmission electron microscopy (TEM, JEM-2100). X-ray photoelectron spectroscopy (XPS) was employed on a PHI5000 Versaprobe - Ⅱ instrument equipped with a C_{1s} (284.8 eV) X-ray source.

2.3. Cell assemble and electrochemical measurement

Cells of CR2032 standard form were assembled to analyze the electrochemical performance. The lithium metal was used as the anode, the positive electrode was prepared by 80% wt $LiNi_xMn_{2-x}O_4$ (active materials), 10% wt carbon black and 10% wt polyvinylidene fluoride (PVDF) in 1-methyl-3-pyrrolidone (NMP) solvent. The electrolyte was 1 M $LiPF_6$ solved in ethylene carbonate (EC), dimethyl carbonate (DMC) and methyl ethyl carbonate (EMC) at a volume ratio of 1:1:1. Galvanostatic cycling was performed between 3.0 and 4.5 V (vs. Li^+/Li) by using Land electric test system CT2001A (Wuhan Jinnuo Electronics Co, Ltd). The cyclic voltammogram (CV) measurements at a scan rate of 0.10 $mV \cdot s^{-1}$ and electrochemical impedance spectroscopy (EIS) measurements in the frequency range of 1.0 Hz to 100 kHz were carried out on an electrochemical workstation (IM6ex, ZAHNER-elektrik GmbH & Co. KG, Kronach, Germany).

3. RESULT AND DISCUSSION

3.1 Structure and morphological analysis

The X-ray diffraction (XRD) patterns of the as-synthesized $LiNi_xMn_{2-x}O_4$ samples are illustrated in Fig. 1. Noted that all the diffraction peaks can be assigned to the $LiMn_2O_4$ (JCPDS No. 35-0782) with a space group of Fd3m [24]. If the tetrahedral sites are occupied by other cations, the (220) peak will appear in the XRD patterns [25]. Therefore, the diffraction peak of (220) cannot be observed in the XRD patterns of Fig.1, which indicates that 8a tetrahedral site is only occupied by Li^+ and the Ni^{2+} are located in the 16d octahedral site. The lattice parameters of all samples are listed in Table 1. Both the lattice parameters and cell volume for all the Ni-doped samples are smaller than that of the pristine $LiMn_2O_4$.

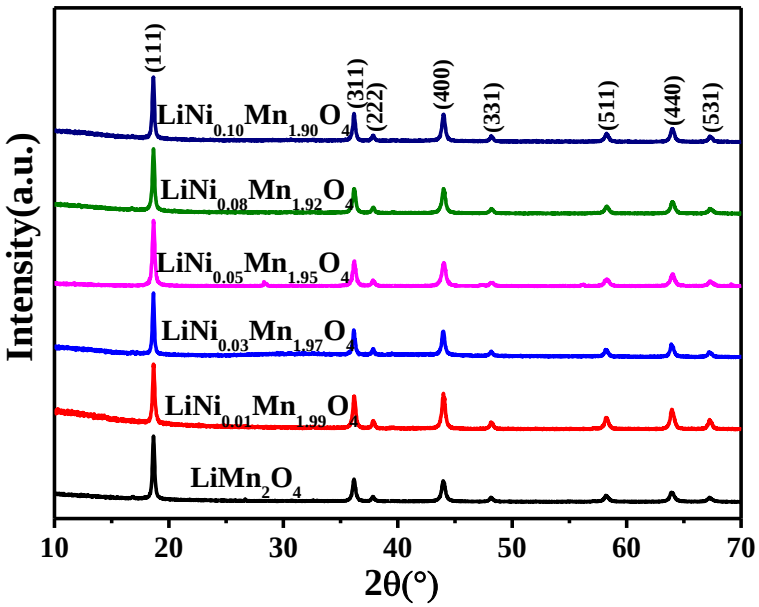

Figure 1. XRD patterns of the $LiNi_xMn_{2-x}O_4$ samples.

Table 1. The lattice parameters of the $LiNi_xMn_{2-x}O_4$ samples

Sample	Lattice constant /Å	Cell volume /Å^3	FWHM (400) peak/°	Position (400) peak /°
x=0	8.232	557.85	0.306	43.958
x=0.01	8.226	556.63	0.259	43.993
x=0.03	8.231	557.64	0.250	43.965
x=0.05	8.221	555.61	0.292	43.983
x=0.08	8.222	555.82	0.289	44.013
x=0.10	8.226	556.63	0.257	43.993

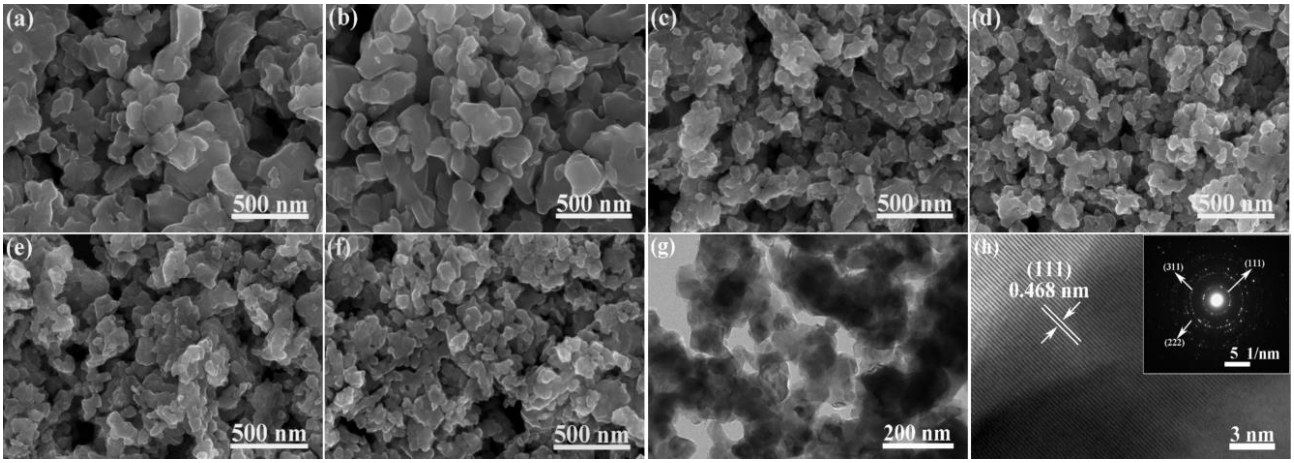

Figure 2. SEM images of the $LiNi_xMn_{2-x}O_4$ samples (a) x=0, (b) x=0.01, (c) x=0.03, (d) x=0.05 and (e) x=0.08, (f) x=0.10, (g) and (h) TEM images and selected area electron diffraction (SAED) patterns of the $LiNi_{0.08}Mn_{1.92}O_4$ sample.

This is mainly because the radius of nickel (II) ions (0.69 nm) is closed to those of Mn ions (Mn^{3+}, 0.65 nm; Mn^{4+}, 0.53 nm) and the bond energy of Ni-O (1029 KJ·mol^{-1}) is stronger than that of Mn-O (946 KJ·mol^{-1}) bond [26]. Furthermore, the (400) peaks of the Ni-doped samples shift toward the higher angle, which is consistent with the decrease of crystal lattice constant. Besides, the FWHM (400) peaks of the Ni-doped samples are smaller than that of undoped $LiMn_2O_4$, indicating that the Ni-doping can exert an important influence on the electrochemical performance.

Fig. 2 (a)-(f) exhibit the SEM images of all samples. As seen, all the samples reveal irregularly-shaped nanoparticles with particle size of 50-80 nm. From the Fig. 2 (a), the agglomeration of the pristine $LiMn_2O_4$ is obvious and the particle size is not uniform. With the increased Ni content from Fig. 2 (b) to (f), the agglomeration was gradually weakened as well as the particle size was decreased correspondingly. This is because the incorporation of Ni^{2+} promotes the formation of crystal nucleus[27], decreases the reunion phenomenon and increases crystallization of all doped samples, which is consistent with the reduction trend of lattice constants in XRD. Fig. 2 g and h show the TEM images of the $LiNi_{0.08}Mn_{1.92}O_4$ sample. As shown, the particles shape is irregular, the octahedral edges is obscure and the crystallinity is relatively poor . The particle size is about 50-80 nm, which is consistent with the SEM result . Fig. 2 (h) further displays the high-resolution TEM and SAED images of the $LiNi_{0.08}Mn_{1.92}O_4$. It presents a set of obvious lattice fringes with d-spacing of 0.468 nm that smaller than the standard (111) facet distance of $LiMn_2O_4$. This is because the bond energy of Ni-O (1029 KJ·mol^{-1}) is stronger than that of Mn-O (946 KJ·mol^{-1}) bond [26], hence resulting the lattice shrinkage. The SAED image shows clear rings consisting of discrete spot, indicating that the nano-$LiNi_xMn_{2-x}O_4$ has an amorphous spinel structure, further demonstrating the poor crystalline , which is consisted with the result of SEM and TEM.

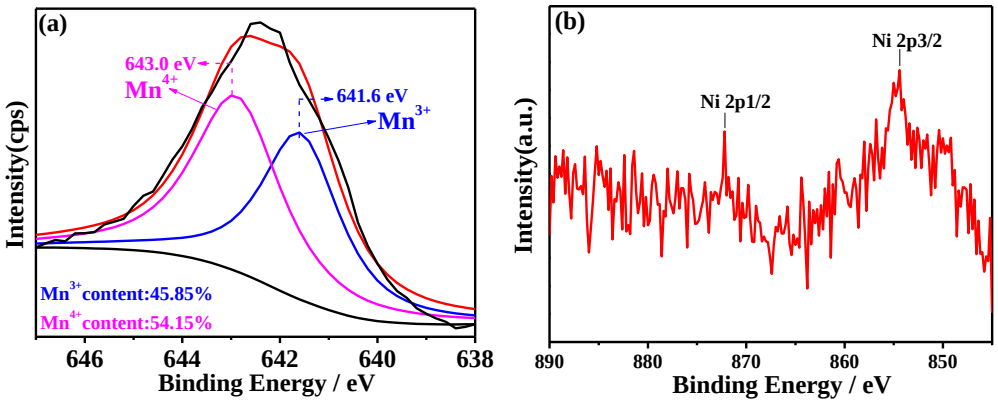

Figure 3. (a) XPS spectrum of $Mn2p_{3/2}$ peak and (b) Ni peak in the $LiNi_{0.08}Mn_{1.92}O_4$.

X-ray photoelectron spectronscopy (XPS) was further employed to analyse the surface compositions and electronic state of the $LiNi_{0.08}Mn_{1.92}O_4$ sample. Fig. 3 (a) show the XPS spectrum of the $Mn2p_{3/2}$ peak in the $LiNi_{0.08}Mn_{1.92}O_4$ sample. The binding energies of ~643.0 eV and ~641.6 eV correspond to the Mn^{4+} and Mn^{3+} in the $Mn2p_{3/2}$ peak. It has been reported by Ding et al [28]. that when the ratio r ($r=[Mn^{4+}]/[Mn^{3+}]$)≧1.18, the Jahn-Teller distortion of the $LiMn_2O_4$ can be inhibited. The value of r and the average valence of Mn ion for $LiNi_{0.08}Mn_{1.92}O_4$ are 1.181 and +3.542, which suggest that

the Ni-doping can restrain the Jahn-Teller effect of the $LiMn_2O_4$ cathode material. In addition, the Fig. 3 (b) also shows the oxidation states of $Ni2p_{1/2}$ (875 eV) and $Ni2p_{3/2}$ (855 eV) [29], respectively, convictively suggesting the existence of Ni element.

3.2 Cyclic stability and rate capacity

In order to evaluate the electrochemical performance, the galvanotactic charge-discharge test was performed at 1 C (1 C= 148.0 $mAh \cdot g^{-1}$) between 3.0-4.5 V. Fig. 4 (a) shows the initial charge-discharge curves of the $LiNi_xMn_{2-x}O_4$ samples.

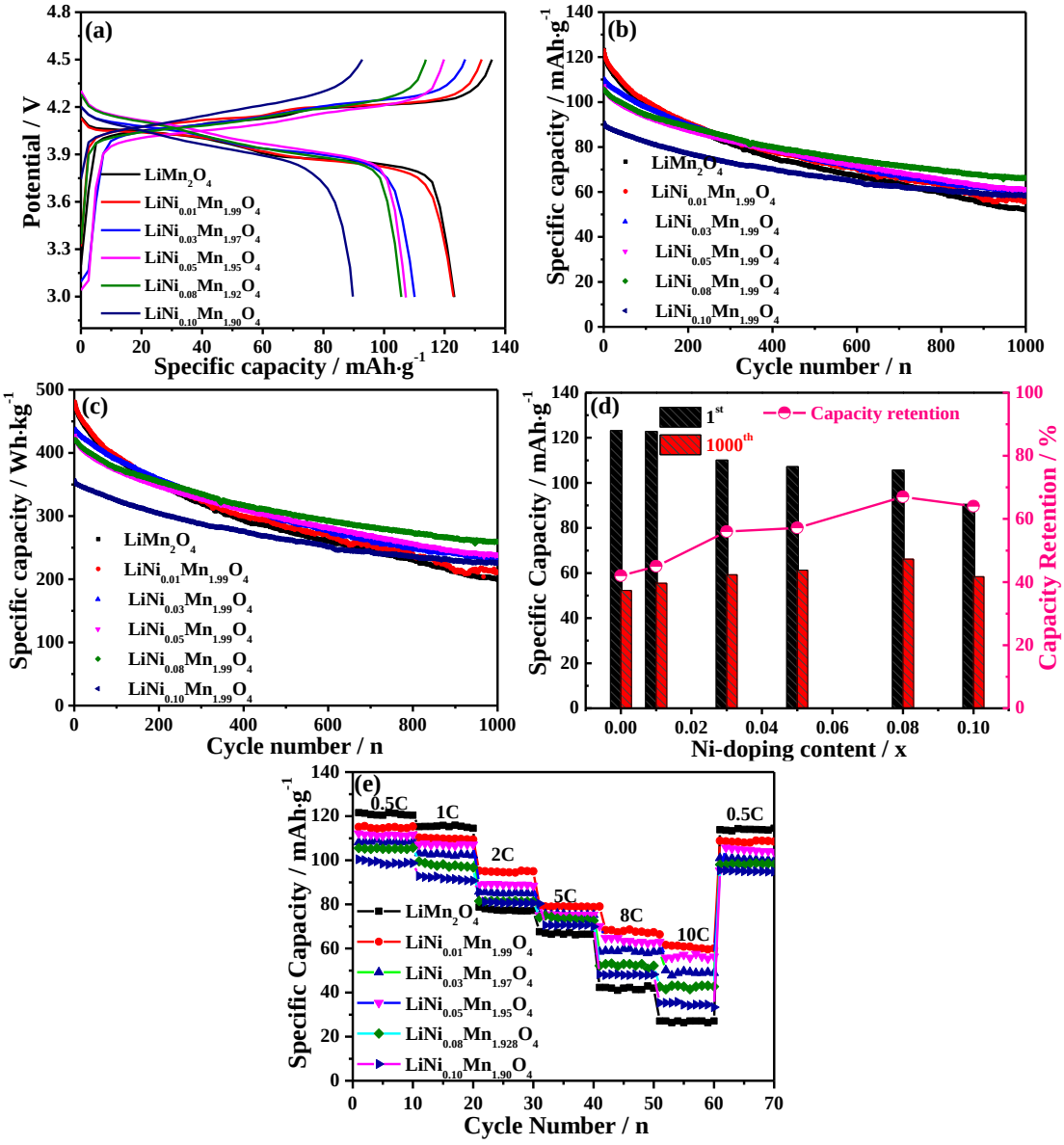

Figure 4. (a) Initial charge-discharge curves of $LiNi_xMn_{2-x}O_4$ samples at 1 C and 25℃, (b) the cyclic performances of $LiNi_xMn_{2-x}O_4$ samples at 1 C and 25℃, (c) mass energy density at 1 C and 25℃, (d) comparison plots of the initial specific capacity and capacity retention rate of $LiNi_xMn_{2-x}O_4$ samples and (e) the rate performance of $LiNi_xMn_{2-x}O_4$ samples.

As shown, all the charge-discharge curves present characteristic voltage plateaus, corresponding to the two-stage intercalation/de-intercalation process of lithium ions, which suggests that incorporating appropriate Ni does not change the electrochemical redox reaction mechanism. Fig. 4 (b) shows the cycling performance of $LiNi_xMn_{2-x}O_4$ at 1 C and 25℃. All Ni-doped samples (except $LiNi_{0.10}Mn_{1.90}O_4$) exhibit the enhanced cycling stability compared to the pristine $LiMn_2O_4$, although the Ni-doped samples sacrifice their initial discharge specific capacities. Such unfavorable outcome could be attribute to the fact that the addition of Ni^{2+} lead to the decrease of active Mn^{3+}. According to the research results[30], the discharge capacity is largely decided by the amount of de-intercalation lithium ions, which depends heavily on the oxidation of Mn^{3+} to Mn^{4+}. Therefore, the Ni-doping has an adverse effect on the initial discharge capacities. To synthetically evaluate the stability of reversible capacity and discharge median-potential as well as the level of packing-density, mass energy density of $LiNi_xMn_{2-x}O_4$ samples is also calculated and displayed in Fig. 4 (c). The optimal $LiNi_{0.08}Mn_{1.92}O_4$ has higher mass energy of 259 $Wh\cdot kg^{-1}$ after 1000 cycles, while the $LiMn_2O_4$ is 225 $Wh\cdot kg^{-1}$. The initial and 1000th discharge specific capacities and capacity retention rates of all samples are summarized in Fig. 4 (d). Notably, the pristine $LiMn_2O_4$ delivers the highest initial discharge specific capacity, however, the capcity sharply fades from 123.0 $mAh\cdot g^{-1}$ to 52.3 $mAh\cdot g^{-1}$, the capacity retention is only 42.0% after 1000 cycles at 1 C. In comparison，the $LiNi_{0.08}Mn_{1.92}O_4$ possesses the relatively high first discharge specific capacity of 105.7 $mAh\cdot g^{-1}$ and the improved retention of 67% after 1000 cycles at 1 C. Fig. 4 (e) compares the rate capacity of all samples at different charge-discharge current densities. Seen that the discharge specific capacities of all cathodes show a downward tendency as the discharge rate increases, which is due to the ohmic polarization and electrochemical polarization that limits the Li^+ diffusion rate[31]. However, the $LiNi_{0.08}Mn_{1.92}O_4$ exhibits better rate capability than that of other samples, its discharge specific capacity is about 70 $mAh\cdot g^{-1}$ at 10 C, while the $LiMn_2O_4$ only delivers about 30 $mAh\cdot g^{-1}$. Thus, the moderate Ni-doping can effectively improve the rate capability.

Table 2. The comparison of the similar cathode materials

Material	Synthesized method	Process conditions	Reference
$LiNi_{0.03}Mo_{0.01}Mn_{1.96}O_4$	hightemperature solid-state method	830℃, 3h	[10]
$LiNi_{0.03}Mg_{0.02}Mn_{1.95}O_4$	microwave technique	800℃, 10min	[11]
$LiNi_{0.1}Al_{0.1}Mn_{1.8}O_4$	solid-state reaction	700℃, 14h	[14]
$LiMn_{1.6}Al_{0.4}O_4$	solution combustion	700℃, 2h	[15]
$LiMn_{1.9}Ni_{0.1}O_4$	low temperature aqueous reduction	780℃, 20h	[21]
$LiNi_{0.2}Mn_{1.8}O_4$	microwave-assisted solid-state reaction	600W-20min, 900℃, 6h	[23]
$LiNi_{0.08}Mn_{1.92}O_4$	one-step solution combustion	500℃, 1h	in this work

Table 2 shows the comparison of the similar cathode materials for $LiMn_2O_4$. Noted that there are

many methods to prepare the $LiMn_2O_4$ cathode materials. Among the above ways, the methods of the doped $LiMn_2O_4$ is complex, the temperature is very high and take a long reaction time. However, in this work, we report a rapid and economical method to synthesize the $LiNi_xMn_{2-x}O_4$ materials.

3.3 Cyclic voltammogram

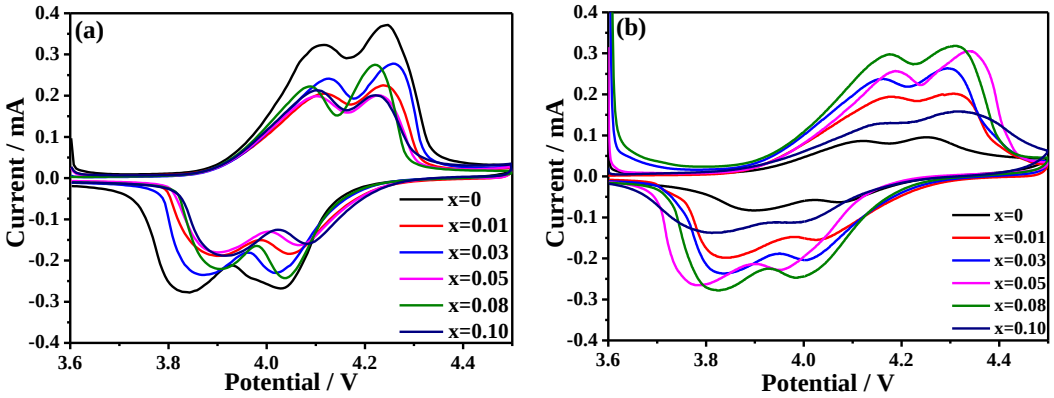

Figure 5. Cyclic voltammetric (CV) curves of $LiNi_xMn_{2-x}O_4$ samples (a) after 1 cycle and (b) after 500 cycles in the potential range of 3.6-4.5 V (vs. Li/Li^+) at a scan rate of 0.1 $mV{\cdot}s^{-1}$.

Fig. 5 (a) and (b) show the cyclic voltammogramic (CV) curves of the $LiNi_xMn_{2-x}O_4$ electrodes after 1 cycle and 500 cycles at 1 C and 25℃ in the potential range of 3.6-4.5 V (vs. Li/Li^+) at a scan rate of 0.1 $mV{\cdot}s^{-1}$, respectively. Noted that two pairs of separated redox peaks can be clearly observed for all materials, which corresponds to the two charge-discharge voltage plateaus (as shown in Fig. 4 (a)), indicating that lithium ions are extracted and inserted from/into the spinel phase by a two-step process[32]. As shown in Fig. 5 (a), both the peak currents and peak areas of the Ni-doped electrodes are not evident except that pristine $LiMn_2O_4$ possesses the largest peak currents and peak areas. After 500 cycles, the redox peaks of all electrodes become more broader and the peak currents is more smaller, as shown in Fig. 5 (b). However, the Ni-doped samples have large peak current and small polarization. Among all samples, the $LiNi_{0.08}Mn_{1.92}O_4$ electrode shows the large peak currents and peak areas after 500 cycles, indicating that the $LiNi_{0.08}Mn_{1.92}O_4$ electrode has better cycle reversibility.

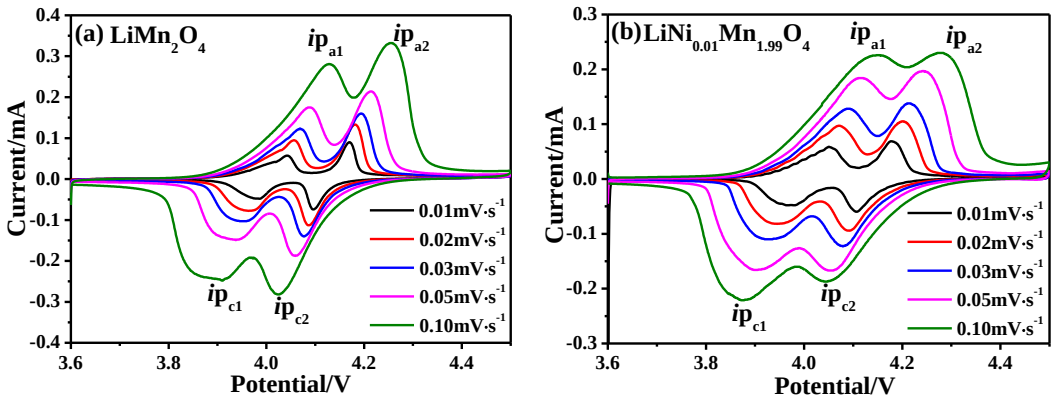

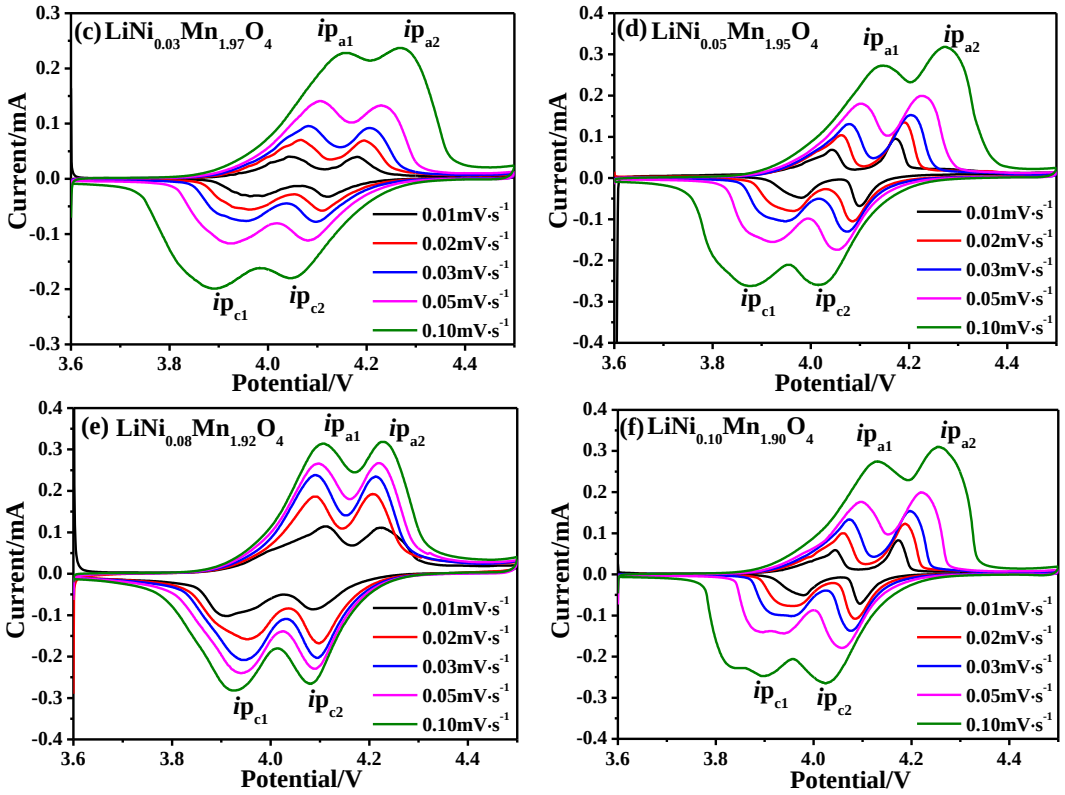

Figure 6. Cyclic voltammetric (CV) curves of $LiNi_xMn_{2-x}O_4$ electrodes in the potential rang of 3.6-4.5 V (vs. Li/Li^+) at different scan rates.

To further study the electrochemical characteristics of the nano-$LiNi_xMn_{2-x}O_4$ ($0 \le x \le 0.10$), Fig. 6 (a)-(f) show a series of cyclic voltammetry at different scan rates in the potential range of 3.6-4.5 V (vs. Li/Li^+). As seen from Fig. 6 (a)-(f), the oxide peak potentials shift to higher values and reductive peak potentials move to lower ones with the increased scan rates, which results from the larger polarization at higher scan rates.

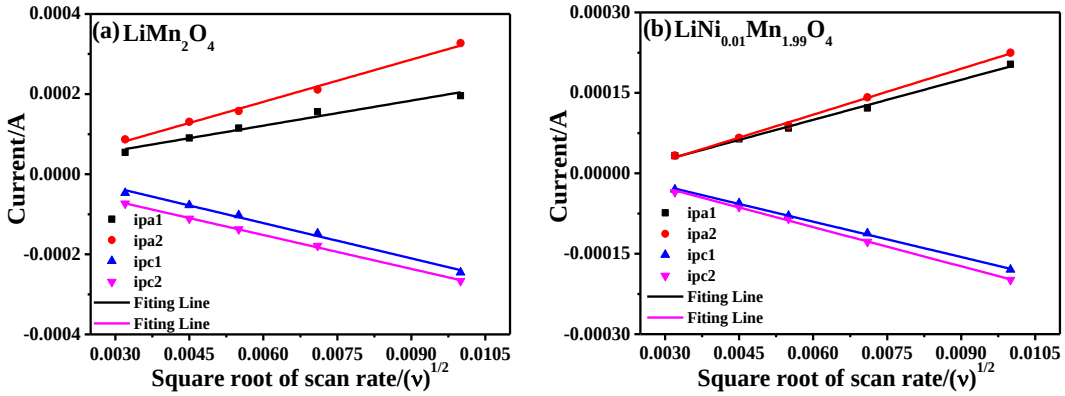

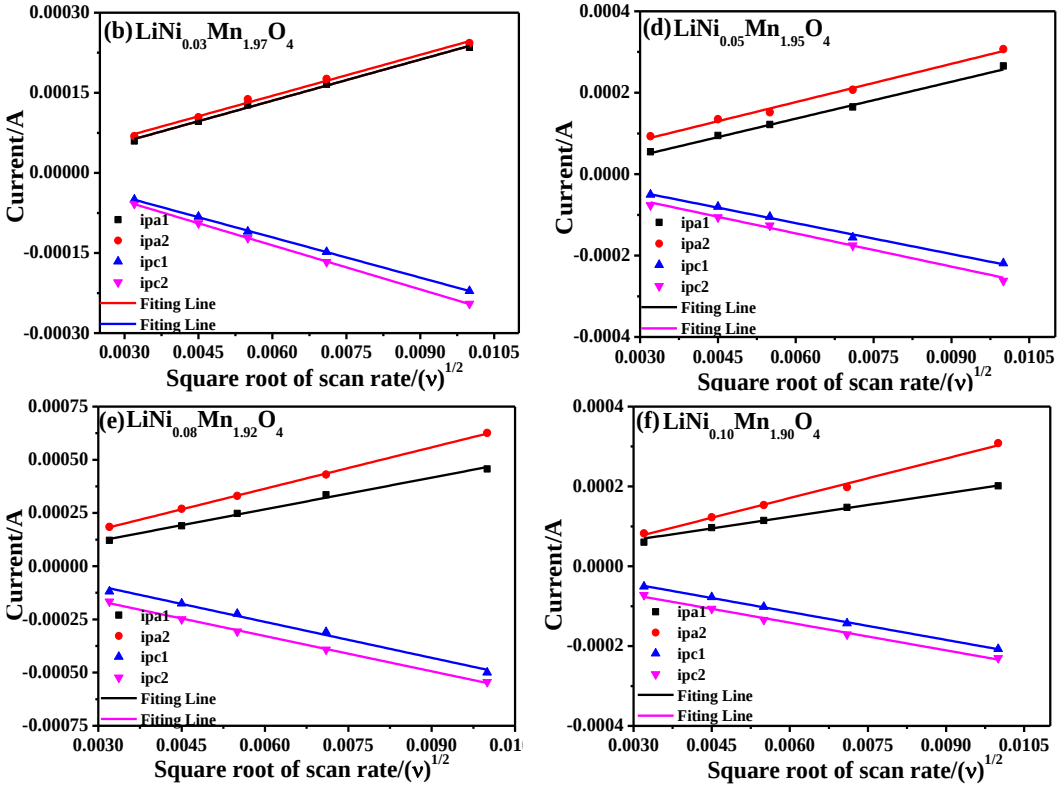

Figure 7. Plots of peak current vs. square root of the scan rate for the $LiNi_xMn_{2-x}O_4$ electrodes.

Table 3. Li^+ diffusion coefficient of $LiNi_xMn_{2-x}O_4$ samples

Electrode	Redox peaks' Li^+ diffusion coefficient, D_{Li+} ($cm^2 \cdot s^{-1}$)			
	ip_{a1}	ip_{a2}	ip_{c1}	ip_{c2}
$LiMn_2O_4$	2.633×10^{-12}	7.473×10^{-12}	5.211×10^{-12}	4.811×10^{-12}
$LiNi_{0.01}Mn_{1.99}O_4$	3.757×10^{-12}	4.924×10^{-12}	2.923×10^{-12}	3.593×10^{-12}
$LiNi_{0.03}Mn_{1.97}O_4$	3.977×10^{-12}	3.959×10^{-12}	3.821×10^{-12}	4.578×10^{-12}
$LiNi_{0.05}Mn_{1.95}O_4$	5.521×10^{-12}	5.941×10^{-12}	3.876×10^{-12}	4.472×10^{-12}
$LiNi_{0.08}Mn_{1.92}O_4$	1.491×10^{-11}	2.535×10^{-11}	1.918×10^{-11}	1.839×10^{-11}
$LiNi_{0.10}Mn_{1.90}O_4$	2.303×10^{-12}	6.579×10^{-12}	3.293×10^{-12}	3.231×10^{-12}

Fig. 7 (a)-(f) give the plots of the peak current vs. square root of the scan rate for all electrodes. The lithium ions diffusion coefficient (D_{Li+}) can be calculated based on the following Randles-Sevcik equation[33]:

$$i_p = (2.69\times10^5)n^{3/2}C_{Li^+}AD_{Li^+}^{1/2}v^{1/2} \quad (1)$$

i_p is the value of peak current (mA), n is the electron transfer number (n≈1 for spinel $LiMn_2O_4$), C_{Li+} is the bulk concentration of Li^+ (given as 0.02378 $mol \cdot cm^{-3}$ for spinel $LiMn_2O_4$), D_{Li+} stands for the Li^+ diffusion coefficient ($cm^2 \cdot s^{-1}$) and v represents the scan rate ($mV \cdot s^{-1}$). The D_{Li+} of redox peaks for all samples can be calculated and listed in Table 3. Noted that the D_{Li+} firstly increases and then decreases with the increasing amount of Ni^{2+} ion. Among them, the $LiNi_{0.08}Mn_{1.92}O_4$ electrode has the larger D_{Li+} than that of other electrodes, indicating the faster lithium ions diffusion in the spinel $LiMn_2O_4$. These

results explain why the $LiNi_{0.08}Mn_{1.92}O_4$ has better electrochemical performance than other electrodes.

3.4 Electrochemical impedance spectroscopy

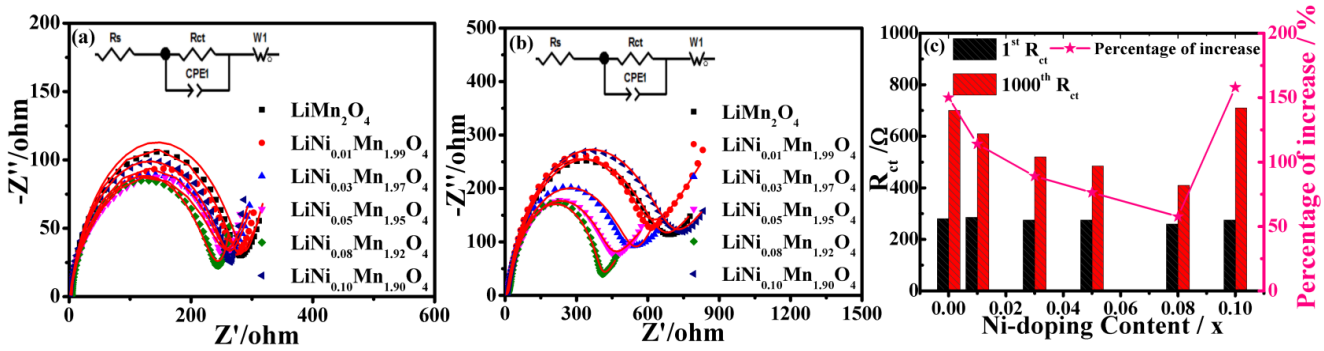

Figure 8. Nyquist plots of $LiNi_xMn_{2-x}O_4$ electrodes (a) before and (b) after 1000 cycles, (c) charge transfer resistance (R_{ct}) at the 1st and 1000th.

The electrochemical impedance spectroscopies (EIS) were measured to analyze the Li^+ diffusion processes. Fig. 8 (a) and (b) present the Nyquist plots of $LiNi_xMn_{2-x}O_4$ electrodes before and after 1000 cycles at 1 C and 25℃, respectively. An equivalent circuit model was used to fit the impedance signal (inset in Fig. 8 (a) and (b)). This circuit included R_s, the ohmic resistance of electrolyte; R_{ct}, the charge transfer resistance; CPE, the double layer capacitance; and W, the Warburg impedance[34,35]. The fitting results of R_{ct} are summarized in Fig. 8 (c). Noted that the R_{ct} of all samples are not obvious before cycling, which is due to the fact that the crystalline is poor and the batteries have been not activated. Thus, lithium ion has the poor diffusion capacity and shows the insignificant difference in the R_{ct}. After 1000 cycles, The R_{ct} value of un-doped $LiMn_2O_4$ increased from 280 Ω to 700 Ω with percentage value of 150.0%. By contrast, the R_{ct} value of $LiNi_{0.08}Mn_{1.92}O_4$ increased from 260 Ω to 410 Ω, with an increase of only 57.7%. All the results suggest that the Ni-doping can effectively reduce the electrode resistance and improve the Li^+diffusion ability[36].

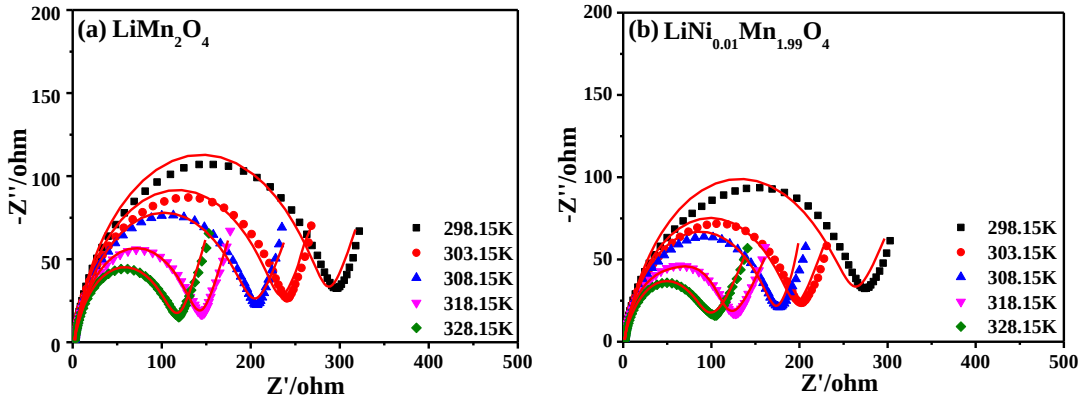

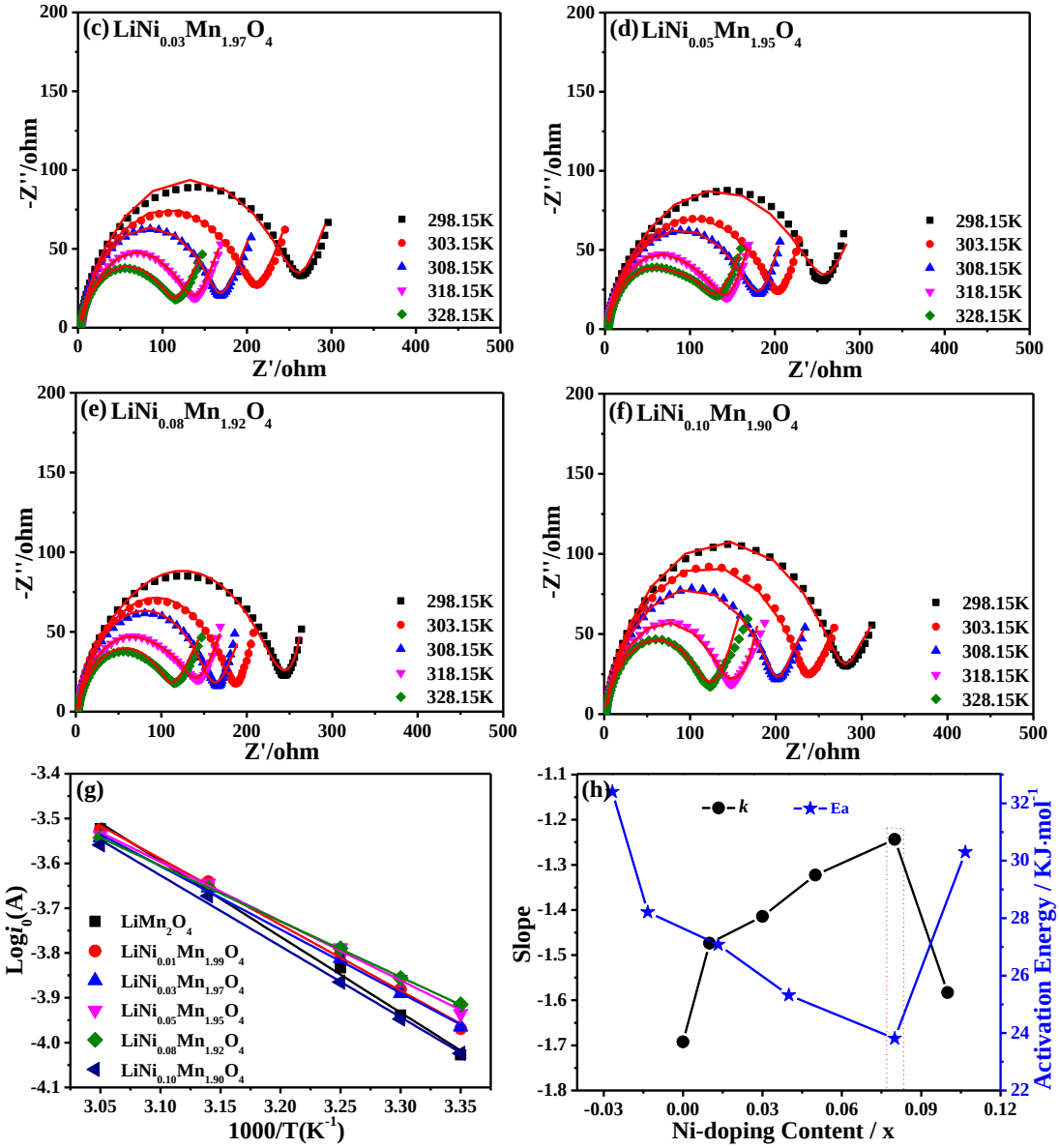

Figure 9 Nyquist plots of (a) pristine $LiMn_2O_4$, (b) $LiNi_{0.01}Mn_{1.99}O_4$, (c) $LiNi_{0.03}Mn_{1.97}O_4$, (d) $LiNi_{0.05}Mn_{1.95}O_4$, (e) $LiNi_{0.08}Mn_{1.92}O_4$, (f) $LiNi_{0.10}Mn_{1.90}O_4$ electrodes at different temperatures, (g) Arrhenius plots of $\log i_0$ vs. 1000/T for $LiNi_xMn_{2-x}O_4$ electrodes and (h) the activation energy of $LiNi_xMn_{2-x}O_4$ samples.

To further explore the electrode kinetic properties, a series of the EIS were performed at different temperatures to calculate the activation energy (E_a) of all samples. Fig. 9 (a)-(f) shows the Nyquist plots for each electrode at different temperatures. The E_a can be calculated on the basis of the following equations [37]:

$$i_0 = RT / nFR_{ct} \quad (2)$$

$$i_0 = A\exp(-E_a / RT) \quad (3)$$

Where, i_0 stands for the exchange current, R represents the gas constant (8.314 $J \cdot mol^{-1} \cdot K^{-1}$), T (K) is the absolute temperature, n is the number of electron transfer (n≈1 for for spinel $LiMn_2O_4$), F is the Faraday constant (96484.5 $C \cdot mol^{-1}$), A is a temperature-independent coefficient. According to the

eq. 2 and eq. 3, the equation of E_a can be expressed: Ea=-R*k*ln10, where k is the slope of the fitting line. The Arrhenius plots of logi_0 as a function of 1000/T of all electrodes are depicted in Fig. 9 (g). Fig. 9 (h) shows the activation energy data and slope of the $LiNi_xMn_{2-x}O_4$ materials. As shown in Fig. 9 (h), the slopes of all samples are increasing firstly and then decreasing with the increasing content of Ni^{2+} ion. In contrast, the E_a is decreasing first and then increasing. Among all samples, the $LiNi_{0.08}Mn_{1.92}O_4$ has the smaller E_a of 23.81 kJ·mol^{-1}. Therefore, doping appropriate Ni ions can effectively decrease the charge transfer resistance, shorten the Li^+ diffusion path and enhance the charge transfer rate, resulting in the reduced energy barrier of Li^+ ions in the migration and diffusion.

4. CONCLUSION

In summary, we have developed a strategy for the synthesis of nano-$LiNi_xMn_{2-x}O_4$ ($0\leq x\leq 0.10$) cathode materials with nonuniform particle size, which was in the range of 50-80 nm. Results revealed that the performance of $LiNi_xMn_{2-x}O_4$ ($0\leq x\leq 0.10$) cathode materials vary significantly with the amount of nickel content. Among Ni-doped samples, the $LiNi_{0.08}Mn_{1.92}O_4$ sample possessed the optimal cycling stability and kinetic properties. It delivered the discharge specific capacity with 66.2 mAh·g^{-1} at 1 C and 25℃ after 1000 cycles, while the discharge specific capacity of pristine $LiMn_2O_4$ was 52.3 mAh·g^{-1}. Moreover, the CV and EIS studies have demonstrated the electrochemical reversibility and kinetic process of $LiNi_{0.08}Mn_{1.92}O_4$. The R_{ct} value of $LiNi_{0.08}Mn_{1.92}O_4$ increased from 260 Ω to 410 Ω after 1000th cycles with an increase of only 57.7%, and it had the smaller apparent activation energy (23.81 kJ·mol^{-1}) and higher lithium diffusion coefficient (1.491×10^{-11} cm^2·s^{-1}). All of above indicated that doping appropriate amount of Ni^{2+} can effectively suppress Jahn-Teller distortion and improve the cycling performance better than $LiMn_2O_4$ systems. The work presented here is reported a facile synthesis method of nano-$LiNi_xMn_{2-x}O_4$ cathode materials. Future research to optimize the cathode's capacity retention and kinetic properties, is currently in progress.

ACKNOWLEDGEMENTS
This work was financially supported by the project for the National Natural Science Foundation of China (51462036，U1602273).

References

1. X. L. Xu, S. X. Deng, H. Wang, J. B. Liu, H. Yan, *Nano-Micro Letters*, 9 (2017)19 .
2. X. L. Xu, C. Y. Qi, Z. D. Hao, H. Wang, J. T. Jiu, J. B. Liu, H. Yan, K. Suganuma, *Nano-Micro Letters*, 9 (2018)10 .
3. B. Z. Chen, B. C. Zhao, J. F. Zhou, J. Y. Song, Z. T. Fang, J. M. Dai, X. B. Zhu, Y. P. Sun, *Journal Solid State Electrochemistry*, (2018)1-10.
4. S. Kalluri, M. Yoon, M. Jo, S. Park, S. Myeong, *Advanced Energy Materials*, 7 (2017) 1601507 .
5. Q. Zhao, L. Ma, Q. Zhang, C. Wang, X. Xu, *Journal of Nanomaterials*, 6 (2015) 6.
6. R. Jiang, C. Cui, H. Ma, T. Chen, *Journal of Electroanalytical Chemistry*, 744 (2015) 69-76.
7. H. Y. Zhao, S. S. Liu, Z. W. Wang, Y. Cai, M. Tan, X. Liu, *Electrochimica Acta*, 199 (2016) 18-26.
8. T. F. Yi, Y. Xie,Y. R. Zhu, R. S. Zhu, M. F. Ye, *Journal of Power Sources*, 211 (2012) 59-65.

9. X. Zhang, Y. Xu, H. Zhang, C. J. Zhao, X. Z. Qian, *Electrochimica Acta*, 145 (2014) 201-208.
10. M. Chen, P. Chen, F. Yang, H. Song, S. Liao, Electrochimica Acta, 206(2016) 356-365.
11. H. Zhang, Y. Xu, D. Liu, X.S. Zhang, C. J. Zhao, Electrochimica Acta, 125 (2014) 225-231.
12. M. W. Xiang, C. C. Peng, L. Zhong, H. L. Bai, C. W. Su, J. M. Guo, *Ceramics International*, 40 (2014) 10839-10845.
13. J. J. Huang, F. L.Yang, Y. J. Guo, C. C. Peng, H. L. Bai, J. M. Guo, *Ceramics International*, 41 (2015) 9662-9667.
14. S. Mukherjee, N. Schuppert, A. Bates, A. Bates, S. C. Lee, S. Park, International Journal of Green Energy, 14 (2017) 1-9.
15. S. A. Akhoon, S. Rubab, M. A. Shah, Materials Research Express, 4 (2017) 10.
16. J. B. Hao, L. Zhong, J. Liu, F. Yang, H. L. Bai, J. M. Guo, *International Journal of Electrochemical Science*, 10 (2015) 4596-4603.
17. M. W. Xiang, C. W. Su, L. Feng, J. M. Guo, *Electrochimica Acta*, 125 (2014) 524-529.
18. A. Iqbal, Y.I qbal, A. M. Khan, S. Ahmed, *Ionics,* 23 (2017) 1995-2003.
19. J. Jiang, G. Gong, C. Li, D. Li, *Nanoscience and Nanotechnology Letters*, 9 (2017) 668-672.
20. N. Kunjuzwa, M. A. Kebede, K. I. Ozoemena, M. K. Mathe, *Rsc Advances*, 6 (2016) 111882-111888.
21. M. A. Kebede, N. Kunjuzwa, C. J. Jafta, M. K. Mathe, K. I. Ozoemena, *Electrochimica Acta*, 128 (2014) 172-177.
22. K. Raju, F. P. Nkosi, E. Viswanathan, M. K.Mathe, K. Damodaran, K. I. Ozoemena, *Physical Chemistry Chemical Physics*, 18 (2016) 13074.
23. F. X. Wang, S. Y. Xiao, Y. Shi, L. L. Liu, Y. S. Zhu, Y. P. Wu, J. Z. Zhang, *Electrochimica Acta*, 93 (2013) 301-306.
24. C. Bellitto, E. M. Bauer, G. Righini, W. R. Branford, A. Antonini, *Journal of Physics and Chemistry of Solids*, 65 (2004) 29-37.
25. Y. L. Cui, W. J. Bao, Z. Yuan, Q. C. Zhang, Z. Sun, *Advanced Materials Research*, 347 (2012) 290-300.
26. P. Singh, A. Sil, M. Nath, S. Ray, *Ceramics Silikaty*, 54 (2010) 38-46.
27. X. Ding, H. Zhou, G. Liu, Z. Yin, Y. Jiang, X. Wang, *Journal of Alloys and Compounds*, 632 (2015) 147-151.
28. Z. Huang, Z. Wang, H. Guo, X. Li, *Journal of Alloys and Compounds*, 671 (2016) 479-485.
29. H. Zhao, S. Liu, Y. Cai, Z. Wang, M. Tan, X. Liu, *Journal of Alloys and Compounds*, 671 (2016) 304-311.
30. W. Wen, S. Chen, Y. Fu, X. Wang, H. Shu, *Journal of Power Sources*, 274 (2015) 219-228.
31. Y. Wang, G. Yang, Z. Yang, L. Zhang, M. Fu, H. Long, *Electrochimica Acta*, 102 (2013) 416-422.
32. Y. Z. Wang, X. Shao, H. Y. Xu, M. Xie, S. X. Deng, H. Wang, *Journal of Power Sources*, 226 (2013) 140-148.
33. H. M. Wu, J. P. Tu, X. T. Chen, Y. Li, X. B. Zhao, G. S. Cao, *Journal of Solid State Electrochemistry*, 11 (2007) 173-176.
34. H. Zhao, F. Li, X. Liu, C. Cheng, Z. Zhang, Y. Wu, *Electrochimica Acta*, 151 (2015) 263-269.
35. R. Singhal, J. J. Saavedra-Aries, R. Katiyar, Y. Ishikawa, M. J. Vikas, S. R. Das, *Journal of Renewable and Sustainable Energy*, 1 (2009)023102.
36. S. L. Chou, J. Z. Wang, H. K. Liu, S. X. Dou, *Journal of Physical Chemistry,* 115 (2011) 16225-16226.